ELSEVIER

# Elastic wave velocities and permeability evolution during compaction of Bleurswiller sandstone

J. Fortin[a],*, A. Schubnel[b], Y. Guéguen[a]

[a]*Ecole Normale Supérieure, Laboratoire de géologie, 24 rue Lhomond 75005 Paris, France*
[b]*Lassonde Institute, 170 College Street, Toronto, ON, Canada M5S3E3*

## Abstract

Field observations and laboratory experiments have recently documented the formation of compaction bands in porous sandstones [Mollema and Antonellini, Tectonophysics 1996;267:209–28; Olsson and Holcomb, Geophys Res Lett 2000;27:3537–40; Bésuelle, J Geophys Res 2001;106:13435–42; Klein et al., Phys Chem Earth 2001;26:21–5]. It has been observed experimentally [Wong et al., J Geophys Res 2001;28:2521–4; Baud et al., J Geophys Res 2003, submitted; Fortin et al., 2003, Abstract EGS-AGU Nice] that under axisymmetric compression, compaction bands develop sub-perpendicular to the main compressive stress which is predicted theoretically in the framework of strain localization theory [Bésuelle, J Geophys Res 2001;106:13435–42; Issen and Rudnicki, J Geophys Res 2000;105:21529–36]. Volumetric strain, fluid transport and elastic properties are intimately coupled to one another, for they all depend on a few intrinsic parameters such as the porosity, the crack density, and the matrix and fluid elastic properties. On the one hand, Scott et al. [Rock Mech Min Sci Geomech 1993;30:763–9] showed that elastic wave velocities were clearly affected during the deformation of porous sandstones. On the other hand, Zhu and Wong [J Geophys Res 1997;102:3027–41] showed that the relation between the evolution of permeability and volumetric strain during compaction of sandstones was not straightforward. In this study, we present for the first time the simultaneous evolution of volumetric strain, elastic wave velocities and permeability for a set of deformation experiments of Bleurswiller sandstone. We show that, although very coherent to one another, those three sets are not systematically correlated. Indeed, inelastic compaction, whether it is distributed or localized, is accompanied by a drastic decrease of elastic wave velocities due to grain crushing, a decrease of permeability and porosity due to pore collapse. Using simple statistical physics concepts based on the study of Kachanov [Adv Appl Mech 1993;30:259–445] and Guéguen and Dienes [Math Geol 1989;21:1–13], we try to understand and address the issue of coupling/decoupling between volumetric strain (mainly sensitive to equant porosity variations), elastic properties (mainly sensitive to crack density) and permeability (theoretically sensitive to both) during the formation of compaction bands. Finally, we show that the mineral composition of a sandstone is a key parameter controlling the effective pressure at which the onset of pore collapse $P^*$ takes place.
© 2005 Elsevier Ltd. All rights reserved.

*Keywords:* Compaction; Compaction bands; Elastic wave velocities; Permeability; Sandstone

## 1. Introduction

Strain localization occurs on all scales in the earth's crust. From the microscale level of grains to fault zones, the deformation of rock mass frequently occurs in narrow, localized bands that can evolve into fracture zones consisting of several bands. Although brittle faulting has generally been associated with dilatancy, recent field observations [1,2] have also focused attention on the formation of compaction bands in porous sandstones. Mollema and Antonellini [2] described those bands in a very porous aeolian sandstone which consisted of thin planar zones of pure compressional deformation, without apparent shear.

*Corresponding author. Tel.: +33 (0) 1 44 32 22 09;
fax: +33 (0) 1 44 32 20 00.

*E-mail address:* fortin@geologie.ens.fr (J. Fortin).

Since then, different laboratory studies [3–6] have documented the occurrence of strain localization in high-porosity sandstones. In particular, the formation of discrete compaction bands was observed in Bentheim sandstone [3] and in Diemelstadt sandstone [7]. Compaction within thin layers was also observed in recent descriptions of borehole breakout [8], which suggests that the phenomenon is pervasive in sandstone formations.

Previous authors [9–11] extended the results of Rudnicki and Rice [12] for high-porosity rocks. These models use a yield surface 'cap' and predict compaction bands under different conditions.

While investigations were conducted on the mechanical behavior of compacted rocks and microstructural observations of deformed samples, there is a paucity of data on the consequences of the development of compaction bands on the physical properties of the rock, i.e. the evolution of the transport and elastic properties.

On the one hand, Vajdova et al. [13] and Holcomb and Olsson [14] showed that permeability across compaction bands was generally reduced by one to two orders of magnitude. Consequently, localized compaction bands may therefore act as barriers to fluid flow in otherwise porous rock and, for example, trap hydrocarbons. However, Zhu and Wong [15] showed that there was no straightforward relation between the evolution of permeability and volumetric strain during the compaction of sandstones.

On the other hand, Scott et al. [16] investigated the evolution of elastic wave velocities during shear-enhanced compaction of Berea sandstone. These authors highlighted the fact that the velocities were clearly being affected at the brittle–ductile transition. However, and once again, the relationship between porosity and elastic properties seemed not to be straightforward and in their data, during triaxial compression test, elastic wave velocities were affected by two distinct and competitive mechanisms. First, elastic wave velocities were correlated to the damage in the rock [17]. Second, as was noted by Schubnel et al. [18], the mean pressure was increasing the velocities due to crack closure and compaction.

In this study, we present for the first time the simultaneous evolution of volumetric strain, elastic wave velocities and permeability for a given set of sandstone samples deformed in a triaxial cell. This sandstone is a 25% porosity Vosgian sandstone, named 'Bleurswiller sandstone'. The experimental program included a set of triaxial compression experiments at confining pressures of 12, 30, 50, 70, 90, 110 MPa. Experiments were performed under wet conditions at a pore pressure of 10 MPa. We present here the complete set of mechanical, elastic wave and permeability data together with microstructural observations of the

samples, allowing identifications of the failure modes. The possible existence of a coupling/decoupling between volumetric strain, elastic properties and permeability is investigated in the discussion using this broad set of results.

## 2. Experimental set-up

The triaxial cell installed in the Laboratoire de Géologie of Ecole Normale Supérieure is made of a pressure vessel, which is a prototype that was designed and constructed by the company Geodesign, based in Roubaix, France. The solid and pore pressure are driven by two hydraulic pumps and two water pumps. The main advantage of this apparatus is the existence of 34 electric feedthroughs which allows the simultaneous measurement of seismic velocities in several directions as well as other properties, such as volume variation and permeability. The first results obtained with this new cell were reported in Schubnel et al. [18].

### 2.1. Description of the vessel

The Geodesign triaxial cell can reach 300 MPa confining pressure (Fig. 1). The confining medium is oil. The confining pressure is servo-controlled with an accuracy of 0.1 MPa thanks to two different pressure sensors: one sensor for the 0–60 MPa pressure range and another one for 60–300 MPa. The pressurization ramp may be as slow as $\sim$0.05 MPa s$^{-1}$.

Axial load is performed through an auto-compensated hydraulic piston (i.e. one that does not move as confining pressure varies). Loading can be both strain rate or stress rate servo-controlled. Taking the piston deformation into account, the minimum strain rate is $10^{-6}$ s$^{-1}$, while the maximum can be up to $10^{-2}$ s$^{-1}$. It is monitored by two DCDTs placed on the top of the piston, outside the vessel. Axial load is servo-controlled with two pressure sensors located outside the vessel. An internal load cell, manufactured by AMC automation, measures the load applied directly on the top of the sample. The axial stress is calculated by dividing the load measured with the internal load cell by the initial cross-sectional area of the sample. We assume that the sample cross-sectional area remains constant throughout the experiment, which is a reasonable approximation within an error of a few percent in stress. The maximum applied stress for 40 mm diameter samples is 717 MPa. The minimum axial stress rate for 40 mm diameter samples is 0.01 MPa s$^{-1}$. Confining and axial pressure systems are given by hydraulic pumps (0–35 MPa) and two intensifiers: (35–300 MPa) for the confining pressure and (35–100 MPa) for the axial stress. The vessel contains a thermocouple for the monitoring of temperature inside the vessel as well as 34 electric wire
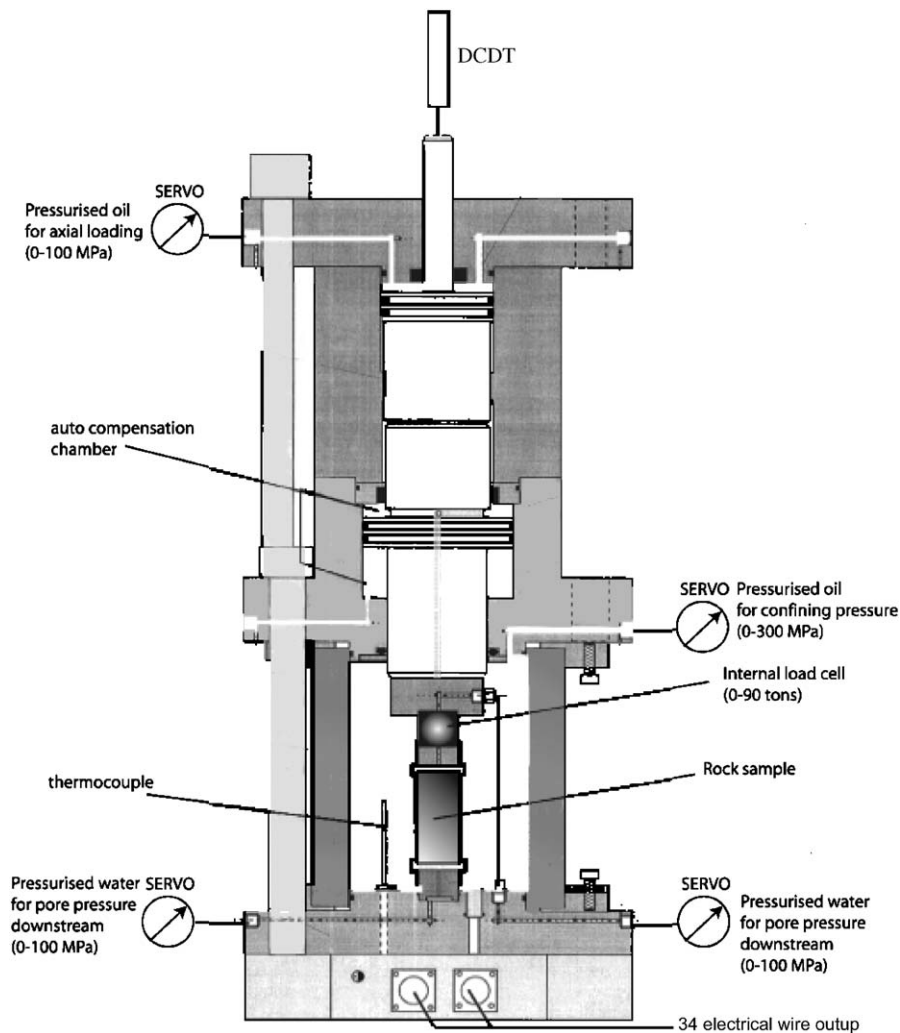
Fig. 1. Schematic diagram of the triX high-pressure cell installed at the Laboratoire de Géologie of Ecole Normale Supérieure.

outputs. Pore pressure is applied using two precision volumetric pumps (Maxitechnologies). Maximum pore pressure is 100 MPa. Both pumps can be controlled either in pressure (0.01 MPa precision, minimum loading rate 1 MPa h$^{-1}$), in flow (minimum flow is 0.1 cm$^3$ h$^{-1}$) or in volume (precision is close to 0.005 cm$^3$). Pore fluid is introduced in the sample through hardened steel end pieces located on the top and bottom of the rock sample.

### 2.2. Description of sample set-up and preparation

The samples were cored from a single Bleurswiller sandstone block, with an initial porosity of 25%. The petrophysical characterization of this Vosgian sandstone is presented in Table 1. The block was obtained from a working quarry located in Frain, France. Seven specimens were cored parallel to the bedding plane. The porosity of each sample was measured using a double saturation technique. The diameter of the rock cylinders was 40 mm and their length 80 mm. Surfaces were

rectified and polished to ensure perfect parallelism and minimum friction during testing. Then, four parallel flat surfaces were saw cut along the cylinder of the sample at 90° to one another.

The samples were saturated with tap water and deformed under fully drained conditions at a constant pore pressure of 10 MPa. Two volumetric pumps kept the pore pressure constant, and the pore volume variations were recorded. During the test, the evolution of the porosity was directly calculated from the total volume variation inside the volumetric pumps. Longitudinal and radial strains were also measured directly on the sample using strain gauges (TML FLA-20, Tokyosokki), each of which was mounted in a 1/4 Wheatstone bridge. In this way, strain measurement accuracy was close to 10$^{-6}$.

*P* and *S* elastic wave velocities were measured perpendicular to the compressional axis, along diameters of the sample, using pairs of source–receivers lead-zirconate piezoceramic tranducers (PZT). PZT

Table 1
Petrophysical description of Bleurswiller sandstone investigated in this study and of Bentheim and Diemelstadt sandstones

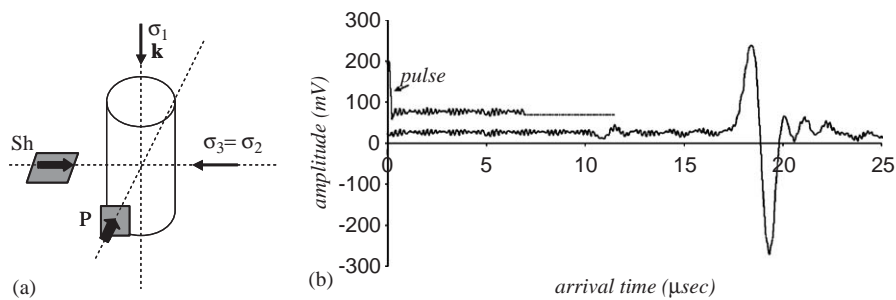| Sandstone | Porosity $\phi$ (%) | Grain radius $R_g$ (μm) | Modal analysis |
|---|---|---|---|
| Bleurswiller | 25 | 112 | Quartz 50%, feldspar 30%, oxides-mica 20% |
| Diemelstadt | 24 | 80 | Quartz 68%, feldspar 26%, mica 2% |
| Bentheim | 23 | 110 | Quartz 95% |



Fig. 2. (a) Schematic view of the ray paths along which the elastic waves are measured in the sample. (b) An example of obtained $S$ waveform. More than 200 signals similar to this one are stacked for each velocity measurement.

(PI255, PI ceramics, 1 MHz resonance frequency) were glued directly on each sample and positioned with 0.5 mm accuracy. $S$ wave velocities are in a horizontal position. The distance between opposite (paired) PZT from which the velocities were calculated was measured within 0.01 mm. Compressional PZT were 10 mm diameters discs, 1 mm thick, and shear PZT were plates (10 × 10 × 1 mm). Pulse was generated by a Sofranel source generator (up to 370 V at 1 MHz frequency).

Acoustic velocities were calculated from the time interval needed for an acoustic pulse to travel across the sample and these were corrected for the steel interfaces of the PZT. For each velocity measurement, more than 200 waveforms were stacked on a digital oscilloscope, in order to increase the signal/noise ratio. In such conditions, the absolute velocity error bar was of the order of a few percent, but relative error in between two consecutive measurements was lowered down to 0.5% thanks to a double picking technique. An example of obtained waveform recordings is shown in Fig. 2.

Once inside the vessel, the sample was covered with a copper jacket to prevent disking and a neoprene jacket which insulated it from the confining oil.

Permeability measurements along the main axis of compression were performed using the steady-state technique: a continuous flow of water (30−300 cm³/h for our samples) provided by the two servo-controlled pumps forced water through the specimen and the pressure gradient between the upstream and downstream provided a measure of $\delta P$. Two symmetrical measures of permeability were performed by switching the flow direction in the sample. Moreover, the permeability values we report in this paper are corrected

from viscosity variations due to temperature, which was recorded by a PT100 gauge.

### 2.3. Experimental procedure

During each experiment, confining pressure was first increased up to 5 MPa. The pore pressure and the confining pressure were then raised simultaneously to 10 and 15 MPa, respectively. The sample was left so during at least 12 h in order to reach full saturation. Finally, confining pressure was slowly increased to the expected pressure. Seven experiments were conducted at confining pressure ranging from 12 to 110 MPa. All triaxial cycles performed in this study were carried out at a constant axial strain rate of $10^{-5}$ s$^{-1}$ and at room temperature. At the end of each experiment, the sample was carefully unloaded for microstructural analysis. Because we were interested in the typology of the localization—dilating shear bands, compacting shear bands or pure compacting bands—we stopped the experiments after a relatively small amount of axial strain (∼3%).

### 3. Experimental data

In the following, we adopt the convention that compressive stresses and compactive strains are positive. The deviatoric stress is noted by $Q = \sigma_1 - \sigma_3$, and the effective mean stress by $P' = (\sigma_1 + 2\sigma_3)/3 - Pp$, where $\sigma_1$ and $\sigma_3$ are the vertically applied (maximum) stress and the confining pressure (minimum) respectively. $Pp$ is the pore pressure and the difference between the

confining pressure ($Pc = \sigma_2 = \sigma_3$) and pore pressure will be referred to as the *effective confining pressure $Pc'$*.

In this section, we present the common evolution of volumetric strain, elastic wave velocities and permeability as measured during the seven experiments we presented in Section 2.3.

### 3.1. Deformation under hydrostatic loading

Our first experiment was performed under isotropic stress conditions. The data obtained during this hydrostatic test are summarized in Fig. 3. Porosity reduction, $P$ and $S$ elastic wave velocities and permeability are plotted versus effective mean stress. The general trend observed in the compaction behavior can be divided into six domains ($A_0 \rightarrow A_1$, $A_1 \rightarrow P^*$, $P^* \rightarrow A_2$, $A_2 \rightarrow A_3$, $A_3 \rightarrow A_4$ and $A_4 \rightarrow A_5$).

The initial non-linear part of the curve ($A_0 \rightarrow A_1$) corresponds to the closure of preexisting cracks in the rock, clearly visible in Fig. 3c and 3d. This domain was characterized by a non-linear increase of both the $P$ and $S$ elastic wave velocities up to an effective mean stress value of 50 MPa. Permeability data are reported against effective mean stress in a semi-log plot (Fig. 3b). During this phase, the permeability remained constant ($k \approx 2.45 \times 10^{-14}$ m$^2$). If the velocities increased in this domain, it is worth noting that the effective mean stress–porosity plot is linear at an effective mean stress of 15 MPa, well below the 50 MPa value when the velocity plateau is observed. Such a domain is characteristic of an extrinsic regime.

In region ($A_1 \rightarrow P^*$), the relationship between effective mean stress and the porosity was linear elastic. In this phase, the elastic wave velocities reached a plateau close to 3900 m/s for $P$ wave and 2275 m/s for $S$ wave and the permeability decreased, in a semi-log plot, linearly (from $k = 2.45 \times 10^{-14}$ to $2 \times 10^{-14}$ m$^2$). Such a domain is characteristic of an intrinsic regime.

The mechanical data (Fig. 3a) show an inflection point which corresponds to the critical effective pressure for the onset of grain crushing and pore collapse $P^*$ [19]. $P^*$ was found to be 135 MPa, a value which was confirmed by a second experiment. Once $P^*$ was reached, accelerated inelastic volume compaction occurred, which was undoubtedly due to extensive grain crushing and pore collapse. This behavior was
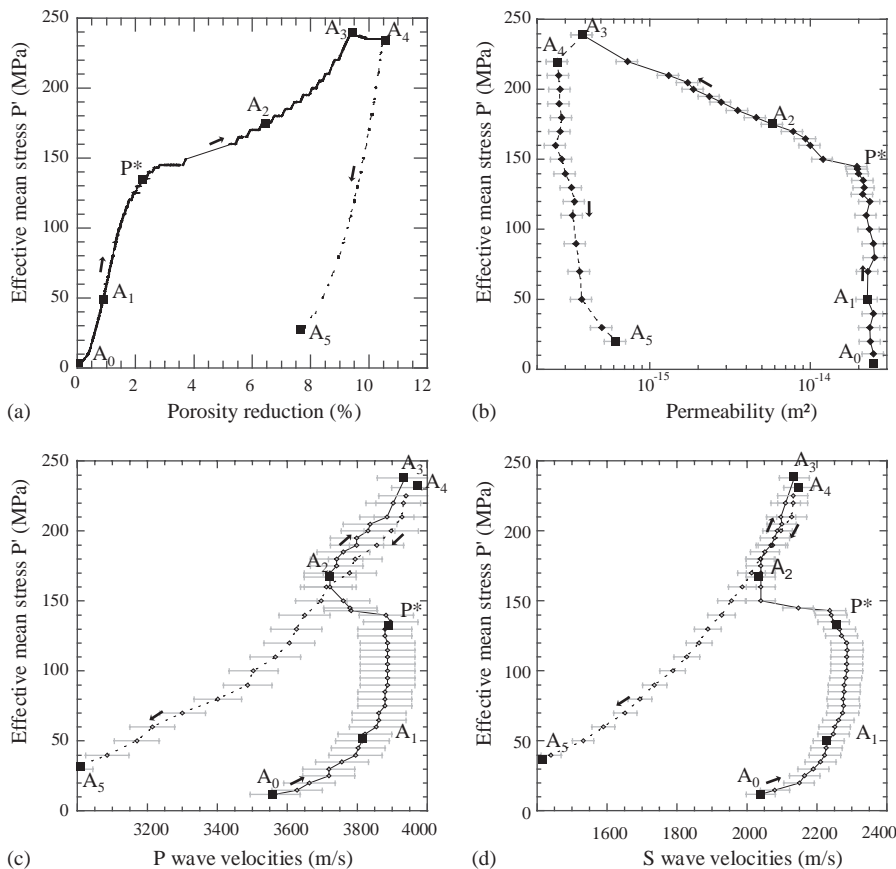


Fig. 3. Hydrostatic loading: (a) effective mean stress versus porosity reduction, (b) effective mean stress versus permeability, (c) effective mean stress versus $P$ wave velocities and (d) effective mean stress versus $S$ wave velocities during hydrostatic test. The different domains that are distinguished in the figure are discussed in the text.

associated with a large decrease of the elastic wave velocities, thus confirming the process of grain crushing. In this domain, $P$ wave velocities decreased by ~4.4% while $S$ wave velocities decreased by ~8.8%. Similarly to the mechanical and elastic properties, the onset of grain crushing was associated with a drastic drop of the permeability of almost one order of magnitude.

The compactive cataclastic flow, which was observed beyond $P^*$, can be separated into two different domains. In the first, the compaction due to the pore collapse and grain crushing was associated with a large decrease of the velocities ($P^* \rightarrow A_2$); however, in the second, the porosity reduction was associated with an increase in elastic wave velocities ($A_2 \rightarrow A_3$). In fact, one can picture on the figure a smooth transition from one domain to the other, with a clear inflection point ($A_2$), where the two micromechanisms balance each other. The first one is pore collapse and porosity reduction, resulting in velocity increase. The second one is grain crushing and crack density increase, which results in velocity decrease. Beyond this point, the second mechanism does not appear to dominate. Moreover, we should add that in this second domain, the newly formed cracks are closed as the material hardened.

It is striking however to note that during the compactive cataclastic flow the permeability decreased, in a semi-log plot, linearly with stress, by almost one order of magnitude. Since during that phase, grain crushing is also creating new crack networks (which would tend to increase permeability, if they were open cracks), one can only assume that the permeability evolution is mainly driven by the equant porosity reduction.

At 245 MPa, we stopped the loading and the sample was left for relaxation[1] overnight. This relaxation phase ($A_3 \rightarrow A_4$) was associated with a porosity reduction of 1%, an increase of both $P$ and $S$ wave velocities and a permeability reduction. Such a behavior is characteristic of visco-elastic restrengthening that can occur during relaxation phases and has been already described in fault gouge materials in terms of an increase of apparent friction coefficient [20] and in limestones and marbles in terms of an increase of elastic properties [18]. However and to our knowledge, the associated decrease in permeability occurring during visco-elastic restrengthening is here observed for the first time.

Finally the sample was slowly unloaded ($A_4 \rightarrow A_5$). As confining pressure was removed, $P$ and $S$ wave velocities decreased linearly by almost 25% and 45%, respectively, because of the opening of the cracks

created during grain crushing and pore collapse. During this last phase, the permeability also increased from $k = 2.6 \times 10^{-16}$ to $6.2 \times 10^{-16} \, \text{m}^2$.

In summary, this figure illustrates very clearly the complex correlation that can exist between macroscopic volumetric strain (mainly sensitive to high aspect ratio voids), elastic properties (mainly sensitive to low aspect ratio voids) and permeability (theoretically sensitive to both) and thus the inter-relations of macroscopic strain, permeability and elastic wave velocities measurements. Indeed, one can see that the correlation is not straightforward, because of the interplay of cracks opening/closing and pore collapse.

### 3.2. Triaxial compression: the brittle regime

The samples deformed at a confining pressure of 12 and 30 MPa are characteristic of the deformation taking place in the brittle regime. Indeed, in these two experiments, the differential stress reached a peak stress followed by macroscopic failure. Rupture was accompanied by a strain softening phase in which the stress progressively dropped to a residual level. Peak stress was observed to increase with confining pressure, which is typical of a Mohr–Coulomb type of brittle failure envelope [21].

The results we obtained during these two experiments are summarized in Table 2 and in Fig. 4 in which porosity, $P$ and $S$ wave elastic velocities and permeability are plotted versus effective mean stress. For reference purposes, hydrostatic data are also plotted in the figure. From the hydrostatic test (Fig. 3), we know that the rock is in the extrinsic regime until the effective mean stress reaches 50 MPa. This result explains why the wave velocities values are higher for the experiment at a confining pressure of 30 MPa than that for the experiment conducted at a confining pressure of 12 MPa. In the same way as we did for the hydrostatic experiment, the mechanical behavior can be divided into three domains.

For the sample deformed at a confining pressure of 30 MPa, the effective mean stress versus porosity reduction was non-linear up to 20 MPa effective mean stress. For the sample deformed at a confining pressure of 12 MPa, the effective mean stress versus porosity

---

[1]Because of the design of the apparatus (see Fig. 1), it is obvious that this relaxation was not a true relaxation phase in the sense of visco-elasticity, but a mix between creep and relaxation, at constant sample + oil volume. However, because the stress decreased from 245 to 235 MPa, we will refer to it as a relaxation phase anyway.

Table 2

Mechanical data for Bleurswiller sandstone samples which failed by shear localization

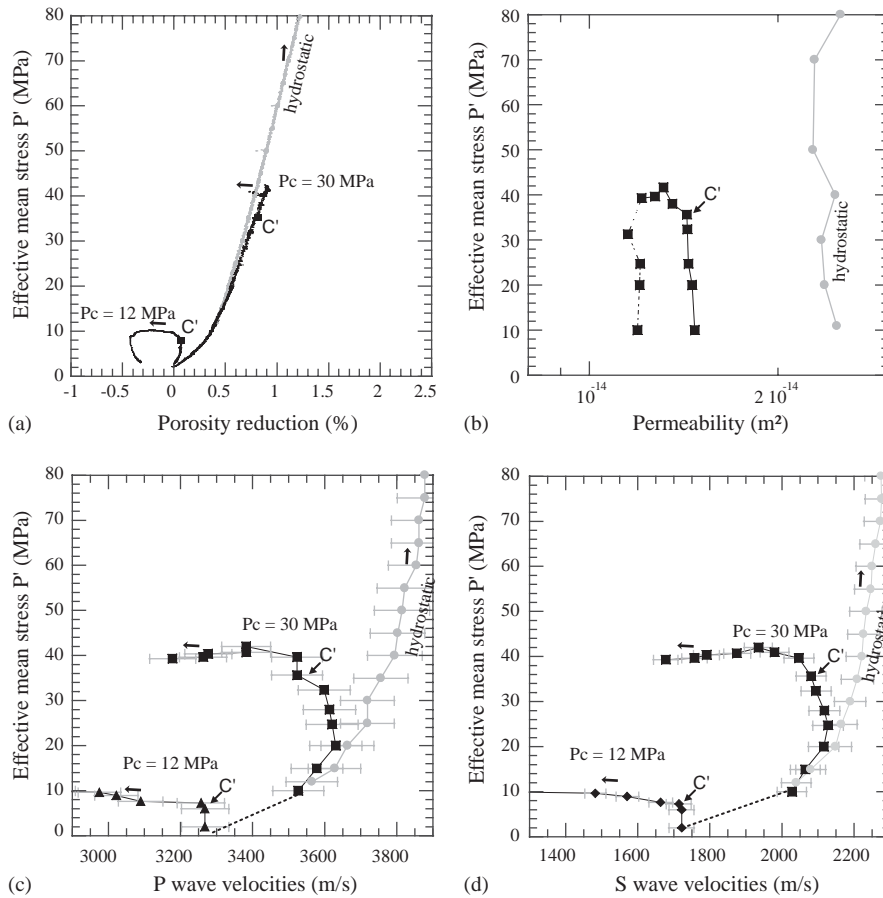| Confining pressure $Pc$ | Effective mean pressure $P'$ at $C'$ | Differential stress $Q$ at $C'$ | Differential stress $Q$ peak stress |
|---|---|---|---|
| 12 | 6 | 16 | 27 |
| 30 | 36 | 48 | 66 |

Fig. 4. The brittle regime: (a) effective mean stress versus porosity reduction, (b) effective mean stress versus permeability, (c) effective mean stress versus $P$ wave velocities and (d) effective mean stress versus $S$ wave velocities for two triaxial compression experiments performed at $Pc = 12$ MPa and $Pc = 30$ MPa.

reduction was non-linear up to 5 MPa effective mean stress. In both cases, this domain was also associated with an increase of the elastic wave velocities due to crack closure.

Then, the rock mechanical response was elastic. $P$ and $S$ wave velocities reached a plateau close to $V_P = 3.6$ km/s, $V_S = 2.1$ km/s and $V_P = 3.25$ km/s, $V_S = 1.72$ km/s for the sample deformed at confining pressures of 30 and 12 MPa, respectively.

For the sample deformed at 12 MPa confining pressure, the onset of cataclastic dilatancy $C'$ was reached at 6 MPa effective mean stress and the rock started to dilate. In this phase, both $P$ and $S$ wave velocities (Fig. 4c, d) decreased drastically, so that 0.5% of macroscopic dilation generated a decrease of more than 10% and 20% for $P$ and $S$ wave velocities, respectively. For the sample deformed at 30 MPa confining pressure, the onset of cataclastic dilatancy $C'$ was reached at 36 MPa effective mean stress. Although the elastic wave velocities decreased drastically, more than 10% and 20% for $P$ and $S$ wave velocities, respectively, no significant macroscopic dilatancy was

observed during that phase. This can probably be explained by the fact that already at such low confinement, dilatancy due to grain crushing with crack formation and compaction due to pore collapse are in competition.

In Fig. 4b, effective mean stress is plotted versus permeability, for the sample deformed at a confining pressure of 30 MPa. It is interesting to note that the cataclastic dilatancy was associated with no visible change in permeability, which is in agreement with the porosity change.

### 3.3. Triaxial compression: localization by shear-enhanced compaction

Under the relatively low confining pressures of 12 and 30 MPa, the mechanical response of Bleurswiller sandstone is characterized by shear-enhanced dilation and brittle faulting. In contrast, for the different tests we conducted at confining pressure ranging from 50 to 110 MPa, the failure mode is associated with appreciable inelastic porosity reduction. Comparing to

the hydrostatic case, the rock samples started to compact beyond a critical stress state noted $C^*$ [22] and from then, strain hardening was observed. Such a deformation is therefore characterized by shear-enhanced compaction [23].

The results for the four experiments we conducted at 50, 70, 90 and 110 MPa confining pressure are summarized in Fig. 5, Tables 3 and 4. In this figure, porosity reduction, $P$ and $S$ wave elastic velocities and permeability are plotted versus effective mean stress. Let us point out that there is a rather good correlation between these different physical parameters obtained in the four experiments. As in the hydrostatic test, different domains can be observed. First, until the effective mean stress reaches 50 MPa, the evolution of the velocities is characteristic of an extrinsic regime: $P$ and $S$ wave velocities increased due to the crack closure until they reached a plateau close to 3.85 km/s for the $P$ wave velocities and 2.2 km/s for the $S$ wave velocities. The second step is characteristic of an intrinsic mechanical behavior: the porosity evolution was linear elastic, the velocities remained constant and the permeability (Fig. 5b) decreased linearly. In all experiments, the onset of

compactive yield $C^*$ was associated with large shear-enhanced compaction. During that phase, the porosity, the elastic wave velocities and the permeability decreased rapidly. For the sample deformed at a 50 MPa confining pressure, 1% of macroscopic compaction generated a decrease of more than 3.8% and 2.8% in $P$ and $S$ wave velocities, respectively. For the sample deformed at 70 MPa, 1% of macroscopic compaction generated a decrease of more than 3.4% and 6% in $P$ and $S$ wave velocities, respectively.

Two points can be underscored here. First, compaction was always associated with a decrease of both $P$

Table 3
Mechanical data for Bleurswiller sandstone samples which failed by compacting-shear bands

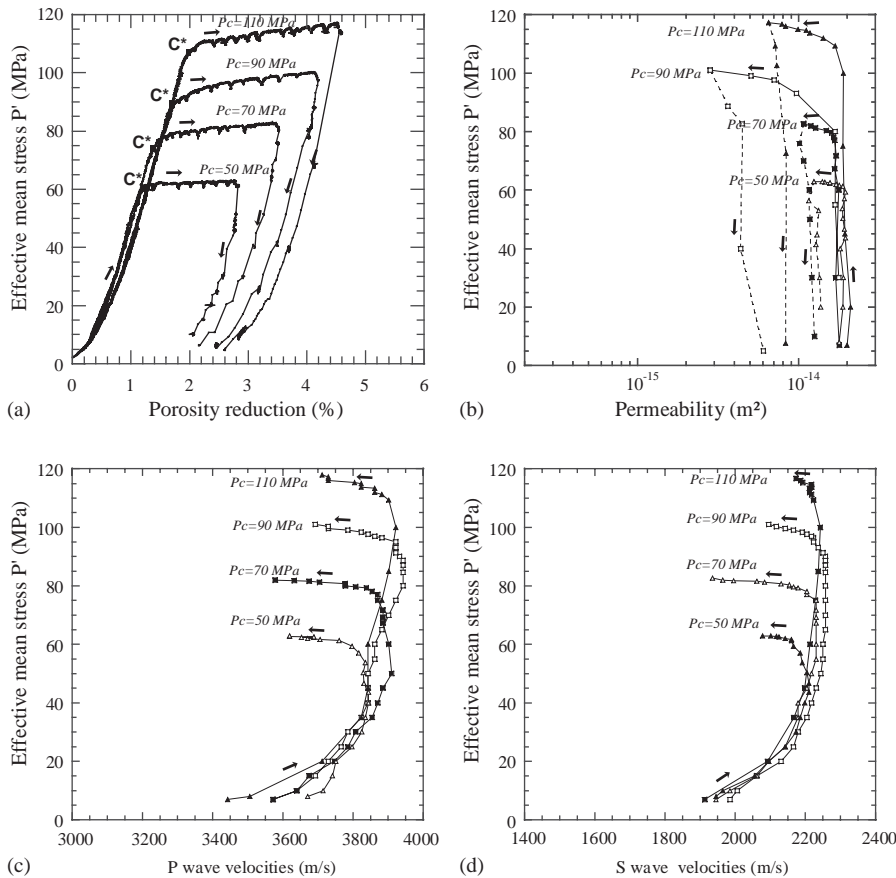| Confining pressure $Pc$ | Effective mean pressure $P'$ at $C^*$ | Differential stress $Q$ at $C^*$ |
|---|---|---|
| 50 | 59 | 57 |
| 70 | 77 | 50 |
| 90 | 90 | 31 |
| 110 | 106 | 19 |



Fig. 5. The ductile or semi-brittle regime: (a) effective mean stress versus porosity reduction, (b) effective mean stress versus permeability, (c) effective mean stress versus $P$ wave velocities and (d) effective mean stress versus $S$ wave velocities for four triaxial compression experiments performed at $Pc = 50$ MPa, $Pc = 70$ MPa, $Pc = 90$ MPa and $Pc = 110$ MPa.

Table 4
Mechanical, permeability, elastic wave velocities data for hydrostatic and triaxial compression experiments on Bleurswiller sandstone

| Effective pressure $P_c - P_p$ (MPa) | Differential stress $Q$ (MPa) | Porosity $\phi$ (%) | Axial strain $\varepsilon^a$ (%) | Permeability $k$ $\times 10^{-16}$ m$^2$ | Waves elastic velocities | |
|---|---|---|---|---|---|---|
| | | | | | $S$ (m/s) | $P$ (m/s) |
| Hydrostatic test—loading | | | | | | |
| 11 | 0 | 24.6 | 0 | 248 | 2040 | 3565 |
| 20 | 0 | 24.4 | 0 | 237 | 2149 | 3663 |
| 30 | 0 | 24.3 | 0 | 234 | 2189 | 3718 |
| 40 | 0 | 24.2 | 0 | 246 | 2222 | 3494 |
| 50 | 0 | 24.1 | 0 | 227 | 2233 | 3814 |
| 70 | 0 | 23.9 | 0 | 228 | 2273 | 3862 |
| 80 | 0 | 23.8 | 0 | 251 | 2274 | 3878 |
| 90 | 0 | 23.7 | 0 | 247 | 2278 | 3886 |
| 100 | 0 | 23.5 | 0 | 232 | 2285 | 3886 |
| 110 | 0 | 23.4 | 0 | 223 | 2285 | 3886 |
| 120 | 0 | 23.2 | 0 | 235 | 2285 | 3886 |
| 125 | 0 | 23.0 | 0 | 211 | 2270 | 3878 |
| 130 | 0 | 22.9 | 0 | 216 | 2264 | 3878 |
| 135 | 0 | 22.7 | 0 | 213 | 2247 | 3894 |
| 140 | 0 | 22.5 | 0 | 200 | 2240 | 3882 |
| 143 | 0 | 22.2 | 0 | 197 | 2237 | 3781 |
| 145 | 0 | 21.6 | 0 | 194 | 2146 | 3779 |
| 150 | 0 | 21.3 | 0 | 120 | 2039 | 3760 |
| 160 | 0 | 19.7 | 0 | 100 | 2039 | 3722 |
| 165 | 0 | 19.4 | 0 | 93.6 | 2039 | 3722 |
| 170 | 0 | 19.0 | 0 | 78.0 | 2039 | 3722 |
| 175 | 0 | 18.5 | 0 | 58.3 | 2039 | 3741 |
| 180 | 0 | 18.2 | 0 | 45.9 | 2039 | 3741 |
| 185 | 0 | 17.8 | 0 | 35.3 | 2051 | 3760 |
| 190 | 0 | 17.5 | 0 | 27.8 | 2068 | 3798 |
| 195 | 0 | 17.2 | 0 | 23.6 | 2079 | 3798 |
| 200 | 0 | 16.9 | 0 | 18.7 | 2087 | 3830 |
| 205 | 0 | 16.6 | 0 | 17.3 | 2099 | 3836 |
| 210 | 0 | 16.4 | 0 | 13.1 | 2097 | 3884 |
| 220 | 0 | 16.1 | 0 | 7.32 | 2111 | 3903 |
| 240 | 0 | 15.6 | 0 | 3.82 | 2134 | 3936 |
| Triaxial test $Pc = 110$ MPa, $Pp = 10$ MPa | | | | | | |
| 7 | 0 | 24.7 | 0 | 199 | 1912 | 3342 |
| 20 | 0 | 24.4 | 0 | 210 | 2092 | 3710 |
| 45 | 0 | 23.9 | 0 | 193 | 2198 | 3842 |
| 75 | 0 | 23.5 | 0 | 189 | 2230 | 3881 |
| 100 | 0 | 23.1 | 0 | 190 | 2242 | 3921 |
| 100 | 26 | 22.8 | 0.3 | 168 | 2223 | 3901 |
| 100 | 36 | 22.3 | 0.82 | 142 | 2211 | 3862 |
| 100 | 39 | 21.9 | 1.2 | 118 | 2217 | 3823 |
| 100 | 42 | 21.5 | 1.38 | 112 | 2217 | — |
| 100 | 44 | 21.3 | 1.8 | 99 | — | 3823 |
| 100 | 48 | 20.8 | 2.3 | 83 | 2186 | 3729 |
| 100 | 50 | 20.7 | 2.51 | 79 | 2174 | 3729 |
| 100 | 52 | 20.4 | 2.78 | 65 | — | 3729 |
| Triaxial test $Pc = 90$ MPa, $Pp = 10$ MPa | | | | | | |
| 7 | 0 | 24.7 | 0 | 160 | 1985 | 3571 |
| 30 | 0 | 24.2 | 0 | 177 | 2179 | 3785 |
| 55 | 0 | 23.8 | 0 | 169 | 2249 | 3861 |
| 80 | 0 | 23.4 | 0 | 168 | 2256 | 3941 |
| 80 | 26 | 23.3 | 0.26 | — | 2256 | 3941 |
| 80 | 30 | 23.2 | 0.31 | — | 2256 | 3931 |
| 80 | 36 | 23 | 0.41 | 97 | 2236 | 3921 |
| 80 | 42 | 22.8 | 0.62 | — | 2223 | 3921 |
| 80 | 47 | 22.6 | 1 | — | 2217 | 3861 |
| 80 | 50 | 22.3 | 1.22 | 70 | 2204 | 3842 |
| 80 | 52 | 22.1 | 1.5 | — | 2191 | 3822 |
| 80 | 54 | 21.8 | 1.81 | 50 | 2166 | 3784 |
| 80 | 60 | 20.8 | 2.92 | 28 | 2094 | 3692 |

Table 4 (continued)

| Effective pressure $P_c - P_p$ (MPa) | Differential stress $Q$ (MPa) | Porosity $\phi$ (%) | Axial strain $\varepsilon^a$ (%) | Permeability $k$ $\times 10^{-16}\,\mathrm{m}^2$ | Waves elastic velocities | |
|---|---|---|---|---|---|---|
| | | | | | $S$ (m/s) | $P$ (m/s) |
| Triaxial test $Pc = 70\,\mathrm{MPa}$, $Pp = 10\,\mathrm{MPa}$ | | | | | | |
| 7 | 0 | 24.7 | 0 | 178 | 1945 | 3571 |
| 30 | 0 | 24.3 | 0 | 170 | 2168 | 3807 |
| 60 | 0 | 23.8 | 0 | 177 | 2230 | 3901 |
| 60 | 22 | 23.7 | 0.13 | 172 | 2230 | 3885 |
| 60 | 35 | 23.7 | 0.29 | 170 | 2230 | 3885 |
| 60 | 45 | 23.6 | 0.42 | — | 2230 | 3869 |
| 60 | 51 | 23.5 | 0.51 | 167 | 2204 | 3870 |
| 60 | 54 | 23.3 | 0.63 | 164 | 2204 | 3854 |
| 60 | 58 | 23.3 | 0.77 | — | 2179 | 3838 |
| 60 | 59 | 23.1 | 0.92 | 159 | 2166 | 3807 |
| 60 | 61 | 22.8 | 1.31 | 148 | 2154 | 3778 |
| 60 | 64 | 22.5 | 1.81 | 127 | 2083 | 3703 |
| 60 | 66 | 21.8 | 2.7 | 118 | 1964 | 3578 |
| 60 | 68 | 21.5 | 3.06 | 107 | 1934 | 3542 |
| Triaxial test $Pc = 50\,\mathrm{MPa}$, $Pp = 10\,\mathrm{MPa}$ | | | | | | |
| 8 | 0 | 24.7 | 0 | 179 | 1945 | 3670 |
| 20 | 0 | 24.5 | 0 | 188 | 2094 | 3750 |
| 30 | 0 | 24.3 | 0 | 189 | 2172 | 3825 |
| 40 | 0 | 24.1 | 0 | 182 | 2197 | 3844 |
| 40 | 11 | 24.08 | 0.12 | 195 | 2210 | 3844 |
| 40 | 20 | 24.06 | 0.22 | 193 | 2210 | 3831 |
| 40 | 31 | 24 | 0.3 | 188 | 2204 | 3829 |
| 40 | 41 | 23.95 | 0.4 | 186 | 2191 | 3834 |
| 40 | 51 | 23.9 | 0.5 | 192 | 2185 | 3815 |
| 40 | 58 | 23.88 | 0.59 | 195 | 2166 | 3796 |
| 40 | 64 | 23.8 | 0.76 | 188 | 2160 | 3759 |
| 40 | 65 | 23.7 | 0.94 | 178 | 2160 | 3705 |
| 40 | 66 | 23.68 | 1.62 | 171 | 2142 | 3670 |
| 40 | 67 | 23.2 | 2 | 107 | — | 3687 |
| 40 | 67.5 | 22.8 | 2.37 | 156 | 2124 | 3687 |
| 40 | 68 | 22.6 | 2.74 | 145 | 2118 | 3618 |
| 40 | 68.5 | 22.4 | 3.12 | 139 | 2100 | 3618 |
| 40 | 68.5 | 22.2 | 3.37 | 120 | 2077 | 3618 |

$^a$Axial strain $\varepsilon$ in the table is the strain due to differential stress during triaxial test; the axial strain during hydrostatic loading is given by $\varepsilon = \Delta\phi/3$.

and $S$ wave velocities. This observation illustrates once again the complex correlation between porosity and elastic properties, which can be only explained by the nucleation of cracks while pores are being closed. The second point is that although the sensors were located in the middle of the sample, the inflection point $C^*$ which marks the critical effective pressure for shear-enhanced compaction is the same for effective mean stress versus porosity reduction and effective mean stress versus elastic wave velocities. Two possible reasons can be proposed as an explanation: first localization onto compaction bands began in the middle of the sample, which in the light of Klein et al. [3] and Olsson and Holcomb [6] studies is unlikely; second, at the onset of shear-enhanced compaction, diffuse compaction is in competition with localization.

Porosity reduction was also associated with a large decrease of the permeability. For the samples deformed at confining pressures of 50 and 70 MPa, at 3% axial strain deformation, the permeability was reduced by a factor of 2, while for the samples deformed at a confining pressure of 90 and 110 MPa, the permeability was reduced by factors of 6.5 and 3.5, respectively. No straightforward quantitative trend of permeability evolution with confining pressure during shear-enhanced compaction can be mapped out.

Fig. 6 plots the deviatoric stress versus the axial strain for the four experiments. In this figure, the large oscillations correspond to points where axial strain was maintained constant and both elastic wave velocities and permeability were measured. During those measurements that never lasted more than 10 min, the deviatoric strain was relaxed quickly, which illustrates the visco-elastic behavior of the rock in the semi-brittle regime. On the other hand, the small oscillations correspond to natural oscillations, possibly due to (1) the volumetric

strain measurements resolution and (2) strain localization and compaction band formation associated with short softening phases as illustrated by Klein et al. [3]. For the sample deformed at 50 MPa confining pressure, the shear-enhanced compaction was characterized by a large value of $C^*$ (in terms of deviatoric stress) and almost no hardening (i.e. purely plastic behavior). In the other experiments, one can see that the value of $C^*$ decreased with confining pressure (as has been widely observed in the literature). In the same way, the strain hardening factor showed positive correlation with confining stress, i.e. the higher confining pressure was, the more material hardened.

## 4. Microstructural data, from dilating-shear bands to pure compacting bands

Fig. 7 is a photograph of Bleurswiller sandstone samples deformed at different confining pressures. A low confining pressure ($Pc = 12$ and 30 MPa) deforma-

tion was localized onto a single discrete fracture plane. At the highest confining pressures ($Pc = 90$ and 110 MPa) deformation localized into several bands perpendicular to the maximum principal stress. We believe those bands correspond to so-called 'compaction band' [2,4,11,5,24]. At confining pressures of 50 and 70 MPa, the macroscopic observation of our samples seemed to show an association of localization bands oriented perpendicular to the maximum principal stress (compaction bands), and slightly oblique localization bands.
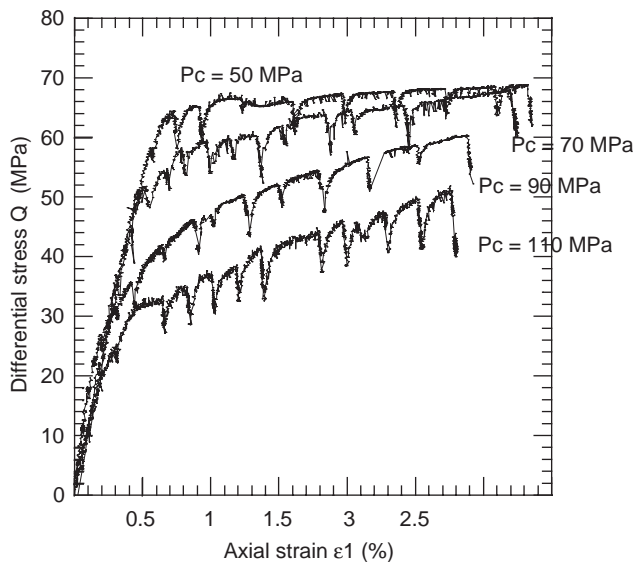
### 4.1. Development of dilating-shear band

The samples deformed at confining pressures of 12 and 30 MPa were observed unloaded using medical X-ray scanner tomography. This technique provides a spatial view over the local density distribution inside the specimen and reveals zones whose density is different from the rest of the specimen. Figs. 8a and b show a slice of the specimens deformed at 12 and 30 MPa confining pressure, respectively.

Shear bands appear as a black area, which implies that their porosity is higher than the material outside the band. It is striking to note that with increasing confining pressure, the dip of the shear band decreased from 75° and 30°, respectively. Such an observation is in good agreement with the orientations found by Bésuelle [25] on another Vosgian sandstone. The thicknesses of the bands are in the range of $400-1000\,\mu m$ whereas a grain radius is around $110\,\mu m$.

### 4.2. Development of compacting-shear bands

We tried to use the same technique in order to observe compaction bands in the other samples, but the differences in the densities in these specimens were too small to obtain a clear spatial view of the localized zones (using the medical parameters).

Fig. 9 corresponds to a series of photograph and optical micrographs illustrating the microstructure inside the sample deformed at 110 MPa confining pressure. In Fig. 9a, more than half of the deformed sample
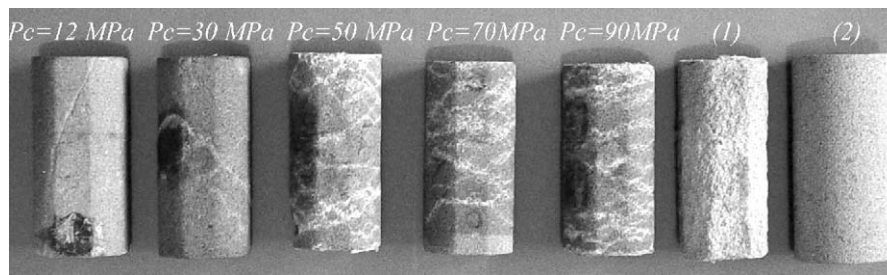


Fig. 6. Differential stress versus axial strain as measured during four triaxial compression experiments performed at $Pc = 50$ MPa, $Pc = 70$ MPa, $Pc = 90$ MPa and $Pc = 110$ MPa.



Fig. 7. Series of photographs picturing the samples of Bleurswiller sandstone deformed at different confining pressure ($Pc$). The diameter of an initial intact sample (2) was 40 mm and the length was 80 mm. (1) is a sample deformed under hydrostatic conditions.
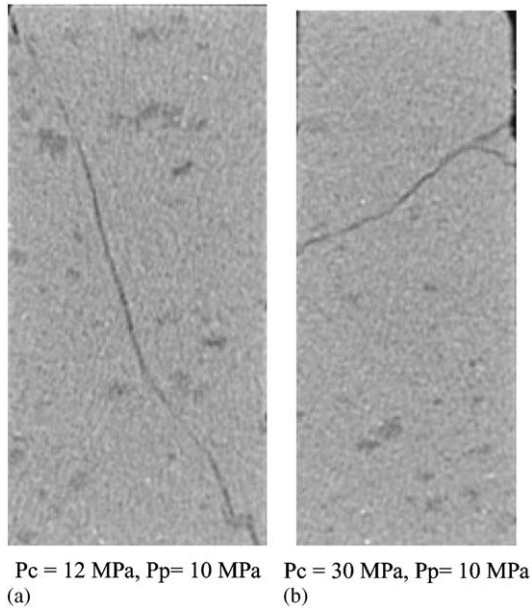
Fig. 8. Localization bands inside specimens tested at confining pressures of 12 MPa (a) and 30 MPa (b). The pore pressure was $Pp = 10$ MPa. Dark areas correspond to shear localization bands that are more porous that the non-damaged rock. The pictures are 8 cm high.

is pictured and the damage in the rock is illustrated by the contrast in colors. Indeed, because the blue epoxy is more absorbed in the fractured zone (due to capillarity), intensive grain crushing appears lighter. Before preparing thin sections, a second blue epoxy was also used in order to fill up the rounded pores. In Fig. 9a, one can distinguish several discrete compaction bands, that are well distributed throughout the sample. The morphology of the sample suggests that compaction bands may have propagated incrementally from the top and bottom to the center. This has been observed by Klein et al. [3] and Olsson and Holcomb [6]. Figs. 9b and c show details of a compaction band as observed in polarized light in optical microscopy. Inside the band, observations show that the material is intensely crushed. Microstructural analysis indicates that the porosity in the bands is only of the order of a few percent, which is to be compared with the 18–23% porosity in the less damaged zones and the 25% initial porosity of the rock. Such features are similar to those observed on Bentheim and Diemelstadt sandstones [3,7,24]. Although Klein et al. [3] speculated that discrete compaction bands are predominant in Bentheim sandstone due to its relatively homogeneous composition (95% of quartz), we document in this study
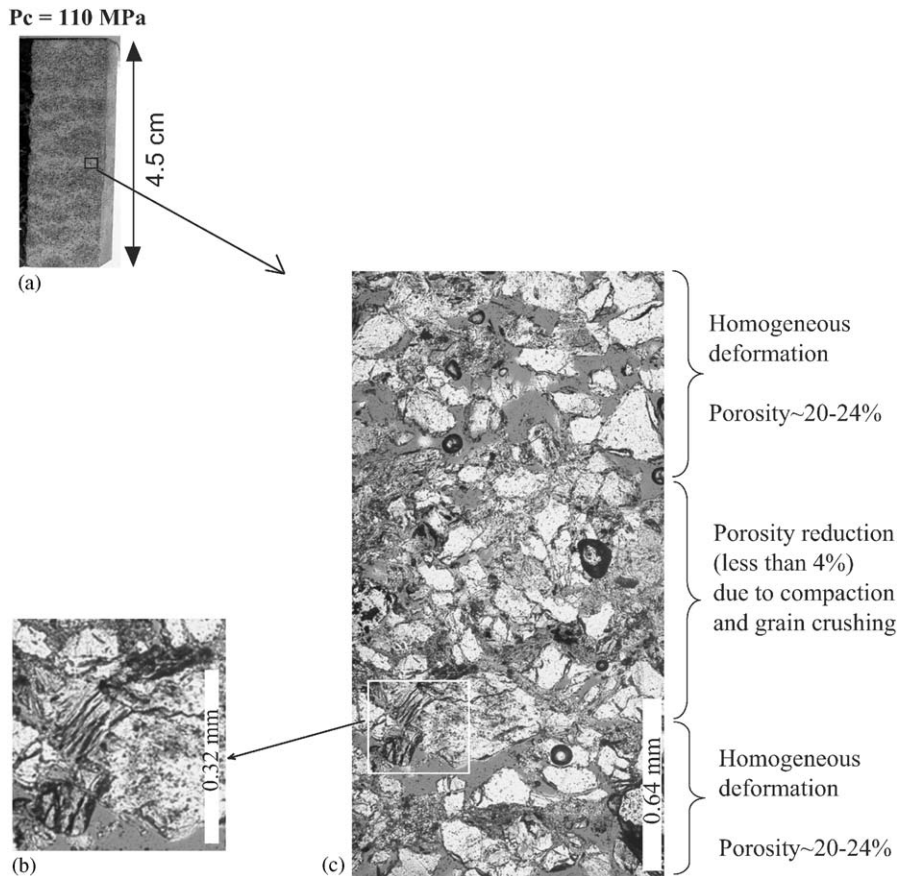


Fig. 9. Compaction bands in the specimen tested at confining pressure of 110 MPa. (a) Full picture of a section in natural light. Principal stress was along the axial direction. (b) Micrographs of the microstructure in polarized light in the optical microscope. This view shows that the average width of a discrete band is ~0.8 mm, which is comparable to the grain size. The micrograph on the left (c) gives a detail of crushed grains inside a band.

that the mechanism of localization of compaction bands also exists in very impure sandstone such as Bleurswiller sandstone. Such an observation suggests that the mineralogical composition may not be an important parameter for the development of discrete compaction bands. However, the microstructure of compacted Bleurswiller sandstone is somewhat different to that observed previously in Diemelstadt and Bentheim sandstones on two points. First, grain crushing seems to be not as extensive as observed in sandstones containing higher proportions of quartz and feldspar. We suspect that a large part of the deformation inside the bands is accommodated by micas and clays which can deform easily into kinks or twins [19]. Second, Figs. 9 and 7 also show that these bands are not linear, but quite tortuous. This might be due again to the fact that the weaker part of the rock is first crushed following maybe a clay–mica path inside the sample during the growth of a band. In any case, further microstructural analysis should be performed. In Particular, SEM microscopy would be of immense interest to observe the deformation of clays and micas inside compaction bands.

## 5. Discussion

In this section, we discuss and compare our results to previously published ones. In terms of elastic properties, we compare our results to those published by Scott et al. [16], in the light of Sayers and Kachanov [17] analysis and Kachanov [26] effective medium models. In terms of permeability, we will compare our results to those obtained on several sandstones by Zhu and Wong [15] and the more recent ones obtained by Vajdova et al. [13]. In terms of the mechanical strength and yield envelopes, we discuss our results in the light of Wong et al. [22], Baud et al. [24], Klein et al. [3] and Tembe et al. [27]. Finally we discuss the interpretation of the onset of grain crushing $P^*$ [19] considered as a possible scaling parameter.

### 5.1. Elastic properties evolution during the compaction of the rocks: towards a dual porosity model

As we have seen in Section 3, elastic wave velocities are strongly affected by two competitive mechanisms during the compaction of porous sandstones. First, elastic wave velocities increase during the inelastic compaction of the rock, due to an increased number of grain contacts and a reduction of the porosity. Such behavior has been widely observed in triaxial experiments performed on a highly porous and poorly compacted assembly of glass spheres [28]. Second, inelastic compaction, whether localized into bands such as in triaxial experiments performed at high confine-

ment, or distributed, such as in hydrostatic experiments, generates a large amount of grain crushing that tends to increase largely the crack density and thus deteriorate the elastic properties of the rock. In spite of the two processes being in competition, our data prove that grain crushing plays the dominant role in controlling elastic properties during inelastic compaction of sandstones. Such an observation is in good agreement with data obtained by Scott et al. [16] in Berea sandstone and its analysis in terms of crack density performed by Sayers and Kachanov [17]. However, Schubnel et al. [29] already noted that because of porosity reduction due to pore collapse, Sayers and Kachanov [17] probably greatly underestimated the increase of crack density that arises at high confinement, when compaction becomes important.

To account for this complexity and following the study of Kachanov [26], the effective Young's modulus of a rock $E_{eff}$ can be written as

$$\frac{E_o}{E_{eff}} = 1 + H\phi \qquad (1)$$

where $E_o$ is the matrix Young's modulus, $\phi$ the porosity and $H$ is a positive scaling parameter that depends on the matrix and fluid properties, the geometry of the inclusions and the interactions between them. The scalar $H$ has been calculated by various authors for all kinds of geometries and fluid properties [30,26,31].

Assuming that the Young's modulus is a bilinear function of both the equant porosity $\phi_r$ and the crack density $\rho$, and assuming noninteractions between those two porosities, Eq. (1) can be re-written in the following form:

$$\frac{E_o}{E_{eff}} = 1 + H\phi_r + h\rho, \qquad (2)$$

where $h$ is a scaling factor that depends on the crack geometry, the fluid and matrix properties and the interactions between the cracks. We do not consider below either complex geometries of pores and cracks, or their interactions. As a first estimate both $H$ and $h$ can be obtained for dry non-interactive pores and cracks. Kachanov's [26] dry isolated spheres model provides an $H$ value equal to 3. In the same way, Kachanov [26] calculated $h$ for randomly distributed dry isolated penny-shaped cracks. In this model [26],

$$h = \frac{16(1 - v_o^2)}{9(1 - v_o/2)}, \qquad (3)$$

where $v_o$ is the Poisson ratio of the solid matrix. Because in most minerals $0.1 < v < 0.3$, Eq. (3) provides an approximate value of $h$ equal to 2. As a consequence, one can see that both $H$ and $h$ values are of the same order of magnitude. Furthermore, it has been shown by various authors [17,29] and by 3D percolation analysis that the crack density in a rock can vary up to 1 or

above 1 close to failure. Because of the intensive grain crushing taking place in compaction bands, it is likely that the crack density is high and close to 1 inside them. Because our triaxial experiments were stopped systematically before shear-enhanced compaction reached 4%, $\phi_r$ only varied by a few percent. These crack density variations are probably of at least one order of magnitude larger than porosity variations. As a consequence, and because the porosity reduction was small in our triaxial experiments, it follows from Eq. (2) that the elastic properties evolution was dominated by grain crushing and the resulting increase in crack density. This suggests that

$$\left(\frac{E_o}{E_{eff}}\right)_{wet} < \left(\frac{E_o}{E_{eff}}\right)_{dry} \approx 1 + 3\phi_r + \frac{16(1 - v_o^2)}{9(1 - v_o/2)}\,\rho. \qquad (4)$$

### 5.2. Permeability evolution during compaction

The relationship between permeability and porosity in a rock is a complex one. It is well known that the permeability depends on many factors including porosity, pore size and aspect ratio distribution, connectivity and tortuosity. One of the main goals of this study is to quantify the impact of compaction bands on fluid flow. In general, we observed that the permeability evolution was consistent with the microstructural observations. Indeed, compaction bands are characterized by a strong reduction of porosity (porosity of less than $\sim5\%$ in the band due to pore collapse and grain crushing, and porosity of $\sim18-24\%$ in the non-damaged zone). These bands are expected to inhibit fluid migration. Our data (Fig. 5b) show a decrease of approximately one order of magnitude in all our triaxial experiments. Moreover, they show that the permeability does not decrease drastically just beyond $C^*$ but more or less linearly with inelastic compaction taking place. These observations as well as microstructural analysis suggest that the bands are not perfectly impermeable. This is so probably because of grain crushing and the existence of a high crack density inside the band. However, the juxtaposition of 'high' and 'low' permeability structures does change the circulation of the fluid inside the rock and similar observations were also recently reported [13]. In their analysis on the permeability evolution during the formation of compaction bands in Bentheim sandstone, Vajdova et al. [13] assumed that the overall permeability of the sample was equal to the permeability of a series of compacted layers embedded in the non-damaged rock. In such a case of a layered media, it simply follows from Darcy's law that the effective permeability of the rock $k_{eff}$ can be written as

$$k_{eff} = \frac{k_m}{(nl/L)(k_m/k_{cb} - 1) + 1}, \qquad (5)$$

where $k_m$ is the permeability of the non-damaged rock, $k_{cb}$ the permeability inside a compaction band, $n$ the number of compaction bands and $l/L$ the ratio between the width of one compaction band and the sample length. Assuming that the permeability ratio between that of the non-damaged rock and that of the compaction bands was of the order of 40–400, they successfully modelled the permeability evolution in their samples for a wide range of confining pressures.

Such an analysis could also be performed in the same way with our data, but here our aim is just to provide some microstructural and physical background to the values obtained for $k_m/k_{cb}$. In the light of Section 3, we have seen that the non-damaged rock permeability is dominated by its rounded pore structure. The closure of preexisting microcracks during preliminary hydrostatic loading did not affect much the overall permeability of the sample. Following the works of Guéguen and Dienes [32], the permeability of highly porous rocks can be represented as that of rock containing tubes. In such a case, the permeability $k_m$ can be written as [33]

$$k_m = \tfrac{1}{32}f\bar{r}^2\phi, \qquad (6)$$

where $\phi$ is the porosity, $\bar{r}$ the average radius of the tubes and $f$ the connectivity factor. Assuming that the connectivity $f$ is 1, the initial porosity being $\phi\sim0.25$ and the initial permeability being $k_m\sim10^{-14}\,\mathrm{m}^2$, Eq. (6) shows that the average pore radius of the idealized equivalent rock is $\bar{r} = \sim1\,\mu\mathrm{m}$. This radius should be interpreted as a 'neck' radius. In the same way, and in the light of Sections 4 and 5.1, we have seen that compaction bands are characterized by highly fractured material. In the case of a highly fractured rock, Guéguen and Dienes [32] showed that the permeability can be represented as that of rock containing penny-shaped cracks. In such a case, the permeability of a compaction band $k_{cb}$ can be written as [33]

$$k_{cb} = \tfrac{2}{15}f\bar{w}^2\bar{\zeta}\rho, \qquad (7)$$

where $\rho$ is the crack density, and $\bar{\zeta}$ and $\bar{w}$ are the crack's average aspect ratio and aperture, respectively. Again $f$ is the connectivity factor. For the sake of simplicity, we can assume that inside the compaction bands, the medium is fully fractured and connected (i.e. $f = 1, \rho = 1$), and that the average crack aperture is approximately equal to the tube aperture we just calculated (i.e. $\bar{w}\sim\bar{r}\sim1\,\mu\mathrm{m}$). Thus, from Eqs. (6) and (7), the ratio $k_m/k_{cb}$ roughly scales as

$$\frac{k_m}{k_{cb}} \sim \frac{\phi}{\bar{\zeta}}. \qquad (8)$$

Consequently, because the characteristic aspect ratio of cracks is $10^{-2}<\zeta<10^{-4}$, the ratio between the initial permeability of a highly porous sandstone and that of a compaction band embedded in the rock is of the order of 6–600. Such a range is comparable to what Vajdova

et al. [13] used to model their permeability evolution in Bentheim sandstone. Their model is therefore also consistent with the previous analysis. Moreover, Eq. (7) also predicts that, because the crack aspect ratios are likely to decrease with increasing confining pressure (because of crack closure), the ratio $k_m/k_{cb}$ is likely to increase with confining pressure. Such an observation seems to be consistent with our data.

### 5.3. Envelopes for brittle strength and compactive shear yield—what actually controls P*?

Data for the brittle strength and compactive yield stress are plotted in the $P$ (effective mean stress) and $Q$ (differential stress) space in Fig. 10. Because we have only two data points for the onset of dilatancy in the brittle regime, the Mohr–Coulomb envelope remains somehow uncertain. However, in the compactive regime data points for the onset of shear enhanced compaction do not map out an ellipse, but rather a straight line. Such an observation seems in contradiction with former studies [22,3,34], which clearly showed that the critical stress levels for the onset of shear enhanced compaction in high-porosity sandstones map out an elliptical yield envelope with a negative slope. A possible explanation is the rock heterogeneity. Fig. 10b shows a slice of an intact specimen, in which one can clearly see different regions with larger porosity (dark areas are more porous). It has been shown recently [27] that in Diemelstadt and Bentheim sandstones, the scattering of the data points on the compactive ellipse can be large and reach 40% for two samples deformed at the same confining pressure, coming from the same block of rock. Again, this might be due to sandstone heterogeneities. As a consequence, experiments on highly porous sandstones should be repeated and performed on samples as large as possible. For another explanation, we can assume that the model of elliptical cap in stress space is not adapted for a sandstone which contains
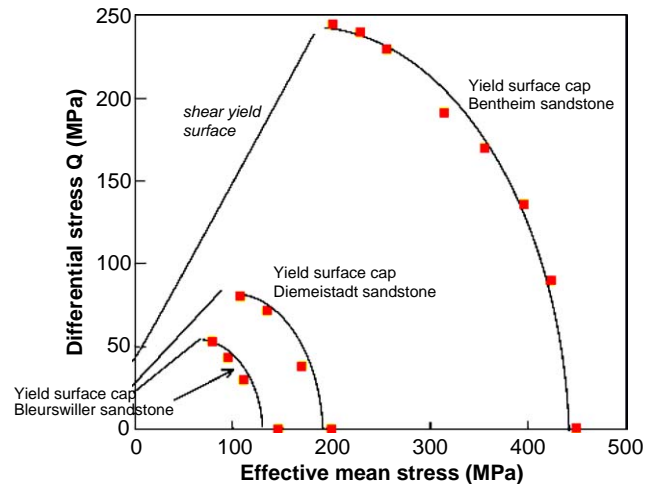


Fig. 11. Comparison between the compactive envelopes (caps) of Bleurswiller (this study), Diemelstadt [7,24] and Bentheim sandstones [3]. The values of $C^*$ at the onset of shear-enhanced compaction are show in the $P$ (effective mean stress) and $Q$ (differential stress) stress space.

about 20% clay. This suggests that more experiments are required to characterize the geometry of the mechanical envelope of Bleurswiller sandstone. This study should only be considered as a preliminary one.

A comparison between our experiments and previous ones on Bentheim and Diemelstadt sandstones [3,34] is however of interest. Fig. 11 plots together in the $PQ$ stress space the compactive yield envelopes of Bleurswiller, Diemelstadt and Bentheim sandstones. Although the porosity and the grain size of these three sandstones are almost identical (Table 1), their strength is very different. Zhang's equation [19] linking $P^*$ to both the grain radius $R$ and the porosity $\phi$ ($P^* \sim (\phi R)^{-3/2}$) cannot account for this result. This implies that there exists another important effect, which could be the mineral composition of the rock. As Bleurswiller sandstone contains about 20% clay, we could suggest that these more deformable minerals lower the yield limit for compaction of this sandstone. SEM microscopy analysis is required to investigate the clay influence on the micromechanics of compaction.

## 6. Conclusion

Confining pressure has a strong influence on the behavior of Bleurswiller sandstone and on the localized deformation structure that develops at failure. We observe two distinct types of failure by localization. For confining pressure up to 30 MPa the response of Bleurswiller sandstone was characterized by shear-enhanced dilation and brittle faulting. For confining pressure in the range from 50 to 110 MPa the response of the sample was characterized by shear-enhanced
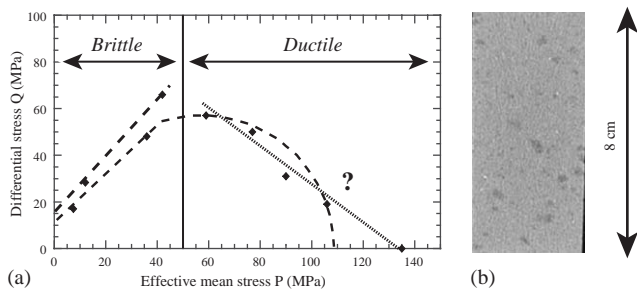


Fig. 10. Envelopes for brittle strength and shear-enhanced compaction: (a) stress state $C^*$ at the onset of shear-enhanced compaction (ductile area), stress state $C'$ at the onset of shear-induced dilation and peak stress for brittle fracture are shown in the $P$ (effective mean stress)–$Q$ (differential stress) stress space. (b) Slice of an intact specimen showing some heterogeneities.

compaction, without faulting. In this second regime, microstructural observations showed that the plastic compaction was localized into bands, called 'compaction bands' [3–6]. The formation of compaction bands was accompanied by a drastic reduction in the both the permeability and the $P$ and $S$ elastic wave velocities.

Elastic properties were clearly shown to be affected by two distinct mechanisms. On the one hand, pore collapse and porosity reduction tend to increase the elastic wave velocities. On the other hand, elastic wave velocities were decreasing because of grain crushing, which was observed to be the dominant factor for inelastic compactive strains smaller than 6% (in agreement with [16]). Such an observation seems to be consistent with most effective medium theory analysis [26].

In the same way, during compactive cataclastic flow, the permeability reduction was observed to be gradual and to increase, in a semi-log plot, linearly with strain. Such an observation had already been reported by Vajdova et al. [13] and interpreted using a simple layered media model. In order to fit their data, these authors showed that the permeability reduction inside compaction bands needed to be of the order of 40–400. Using a statistical physics approach, based on the works of Guéguen and Dienes [32], we showed that the ratio between the permeability inside a compaction band $k_{cb}$ and that of the intact rock $k_m$ was simply controlled by the initial porosity $\phi$ and the crack's average aspect ratio $\zeta$ inside the band in the following way: $k_m/k_{cb} \sim \phi/\zeta$. This theoretical result is in agreement with both our study and Vajdova et al. [13].

Compared with previous studies performed on Diemelstadt [24] and Bentheim sandstones [3], we could note some major differences. First, although all three sandstones showed roughly the same initial porosity and grain size, their strength in isotropic compression was observed to vary from 135 MPa in Bleurswiller sandstone to 390 MPa in Bentheim sandstone. Such differences, which contradict Zhang et al.'s [19] law, is probably due to the difference in composition of these sandstones.

Second, the compactive yield envelope that we depicted in Bleurswiller sandstone does not map out an elliptical cap in the principal stress space [22], which is an intriguing result. Further experiments are required in order to confirm the shape of the envelope and improve our understanding of Bleurswiller sandstone behavior. SEM microscopy will hopefully also permit to clarify the role of clays in the micromechanics of compaction. In perspectives, we showed that the evolution of elastic wave velocities depended on two mechanisms which could be quantified more precisely. The influence of the stress path in the process of localization also seems to be a key issue lately raised by

theoretical work performed by Grueschow et al. [35]. Our apparatus at ENS is designed for such complex experimentations.

## References

[1] Antonellini M, Aydin A, Pollard D. Microstructure of deformation bands in porous sandstones at Arches National Park, Utah. J Struct Geol 1994;16:941–59.

[2] Mollema P, Antonellini M. Compaction bands: a structural analog for anti-mode I cracks in aeolian sandstone. Tectonophysics 1996;267:209–28.

[3] Klein E, Baud P, Reuschlé T, Wong T-F. Mechanical behaviour and failure mode of Bentheim sandstone under triaxial compression. Phys Chem Earth 2001;26:21–5.

[4] Wong T-F, Baud P, Klein E. Localized failure modes in a compactant porous rock. J Geophys Res 2001;28:2521–4.

[5] Olsson W. Quasistatic propagation of compaction fronts in porous rocks. Mech Mater 2001;33:659–68.

[6] Olsson W, Holcomb D. Compaction localization in porous rock. Geophys Res Lett 2000;27:3537–40.

[7] Fortin J, Baud P, Wong T-F. Mechanical compaction of Diemelstadt: from compacting shear bands to pure compaction bands. Abstract EGS-AGU Nice 2003.

[8] Haimson B. Fracture-like borehole breakouts in high porosity sandstone: are they caused by compaction bands? Phys Chem Earth A 2001;26:15–20.

[9] Issen K, Rudnicki J. Conditions for compaction bands in porous rock. J Geophys Res 2000;105:21529–36.

[10] Olsson W. Theorical and experimental investigation of compaction bands in porous rock. J Geophys Res 1999;104:7219–28.

[11] Bésuelle P. Compacting and dilating shear bands in porous rock. J Geophys Res 2001;106:13435–42.

[12] Rudnicki J, Rice J. Conditions for the localization of deformation in pressure-sensitive dilatant materials. J Mech Phys Solids 1975;23:371–94.

[13] Vajdova V, Baud P, Wong T-F. Permeability evolution during localized deformation in Bentheim sandstone. Submitted.

[14] Holcomb D, Olsson W. Compaction localization and fluid flow. J Geophys Res 2003;108(B6):2290–303.

[15] Zhu W, Wong T-F. The transition from brittle faulting to cataclastic flow in porous sandstone: permeability evolution. J Geophys Res 1997;102:3027–41.

[16] Scott T, Ma Q, Roegiers J-C. Acoustic velocity changes during shear enhanced compaction of sandstone. Rock Mech Min Sci Geomech 1993;30:763–9.

[17] Sayers C, Kachanov M. Microcrack induced elastic wave anisotropy of brittle rocks. J Geophys Res 1995;100:4149–56.

[18] Schubnel A, Fortin J, Burlini L, Guéguen Y. Damage and elastic recovery of calcite-rich rocks deformed in the cataclastic regime. Geol Soc London (special edition on High Strain Zone), in press.

[19] Zhang J, Wong T-F, Davis D. Micromechanics of pressure induced grain crushing in porous rock. J Geophys Res 1990;95:341–52.

[20] Beeler N, Tullis T. The role of time and displacement in velocity-dependent volumetric strain of fault zones. J Geophys Res 1997;102:22595–609.

[21] Paterson M. Experimental rock deformation—the brittle field. Berlin: Springer; 1978.

[22] Wong T-F, David C, Zhu W. The transition from brittle faulting to cataclastic flow in porous sandstone: mechanical deformation. J Geophys Res 1997;102:3009–25.

[23] Curran J, Carroll M. Shear stress enhancement of void compaction. J Geophys Res 1979;84:1105–12.

[24] Baud P, Klein E, Wong T-F. Compaction localization in porous sandstone: spatial evolution of damage and acoustic emission activity. J Struct Geol 2004;26: 603–24.

[25] Bésuelle P. Evolution of strain localisation with stress in a sandstone: brittle and semi-brittle regimes. Phys Chem Earth 2001;26:101–6.

[26] Kachanov M. Elastic solids with many cracks and related problems. Adv Appl Mech 1993;30:259–445.

[27] S. Tembe, P. Baud, T. Wong, Development of discrete compaction bands in two porous sandstones. Eos Trans AGU 84(46) (2003) Abstract T41D-0253.

[28] Domenico S. Elastic properties of unconsolidated porous sand reservoirs. Geophysics 1977;42:1339–68.

[29] A. Schubnel, Y. Gueguen, Dispersion and anisotropy of elastic waves in cracked rocks. J Geophys Res 108.

[30] Mukerji T, Mavko G. Pore fluid effects on seismic velocity in anisotropic rock. Geophysics 1998;59:233–44.

[31] Mavko G, Mukerji T, Dvorkin J. The rock physics handbook. Cambridge: Cambridge University Press; 1998.

[32] Guéguen Y, Dienes J. Transport properties of rocks from statistics and percolation. Math Geol 1989;21:1–13.

[33] Guéguen Y, Palcauskias V. Introduction to the physics of rocks. Princeton, NJ: Princeton University Press; 1994.

[34] Baud P, Schubnel A, Wong T-F. Dilatancy, compaction, and failure mode in Solnhofen limestone. J Geophys Res 2000;105: 19289–303.

[35] Grueschow E, Rudnicki J. Modeling constitutive behavior and compaction localization for high porosity sandstone. Eos Trans AGU 84(46) (2003) Abstract T42A-0279.